RESEARCH ARTICLE

Development of Dual-Unit Ceiling Adhesion Robot System With Passive Hinge for Obstacle Traversal Under Kinodynamic Constraints

YOUNG-WOON SONG[1], **JUNGILL KANG**[1], **AND SON-CHEOL YU**[2], (Member, IEEE)

[1]Department of Convergence IT Engineering, Pohang University of Science and Technology (POSTECH), Pohang 37673, South Korea
[2]Division of Advanced Nuclear Engineering, Pohang University of Science and Technology (POSTECH), Pohang 37673, South Korea

Corresponding author: Son-Cheol Yu (sncyu@postech.ac.kr)

ABSTRACT The inspection of high ceilings or surfaces is important to ensure the quality and safety of infrastructure; however, the approach adopted by people or conventional robots is rather limited. Kinodynamic constraints (simultaneous kinematic and dynamic constraints) are presented by obstacles in real-life scenarios, such as suspended piping and wiring, which further limits the usability of robots. Therefore, this paper proposed an adhesion robot system that is attached to and maneuvers on flat and curved ceilings while traversing obstructions. To traverse obstacles, the robot comprises two units connected by a passive hinge mechanism. Traversal motion is achieved under adhesion force control with preexisting electric ducted fans without using separate hinge motors; thus, no additional weight is included. In addition to robot hardware, this study investigated the development of a control method based on dynamic analysis under the aforementioned kinodynamic constraints. Specifically, the proposed control algorithm considers the slipping and rollover conditions of the robot caused by the external force and moment applied to the unit during the obstacle traversal, respectively. The algorithm was systematically analyzed by conducting simulations to prevent the robot from experiencing adhesion failure, and the results were verified experimentally. The use of the robot in real-life scenarios was determined by performing feasibility tests in real-life applications.

INDEX TERMS Ceiling inspection, climbing robot, dynamic analysis, electric ducted fan, kinodynamic constraint, mobile robot, passive hinge.

I. INTRODUCTION

Over the past few decades, various robots that adhere to and maneuver on surfaces have been developed to perform different tasks, such as inspection and cleaning of surfaces. These include the structures of nuclear power plants [1], [2], external surfaces of buildings [3], [4], and social infrastructure such as tunnels and bridges [5], [6]. To perform tasks on these surfaces, the robot must satisfy the following requirements: First, it should be firmly attached to the surface

The associate editor coordinating the review of this manuscript and approving it for publication was Aysegul Ucar.

of interest so that the tasks can be executed in a stable manner. Second, the robot should be able to move precisely along the surface for a precise inspection. Third, short-distance imaging capability is essential to accurately quantify structural damage by capturing small cracks or defects on the inspection surface [7].

Climbing robots often satisfy these requirements, and although the use of an aerial drone can be considered in simple inspection tasks employing cameras, conventional drones cannot be firmly attached to a surface of interest, and are unsuitable for precise movement and imaging at short and constant distances. In contrast, for climbing robots,
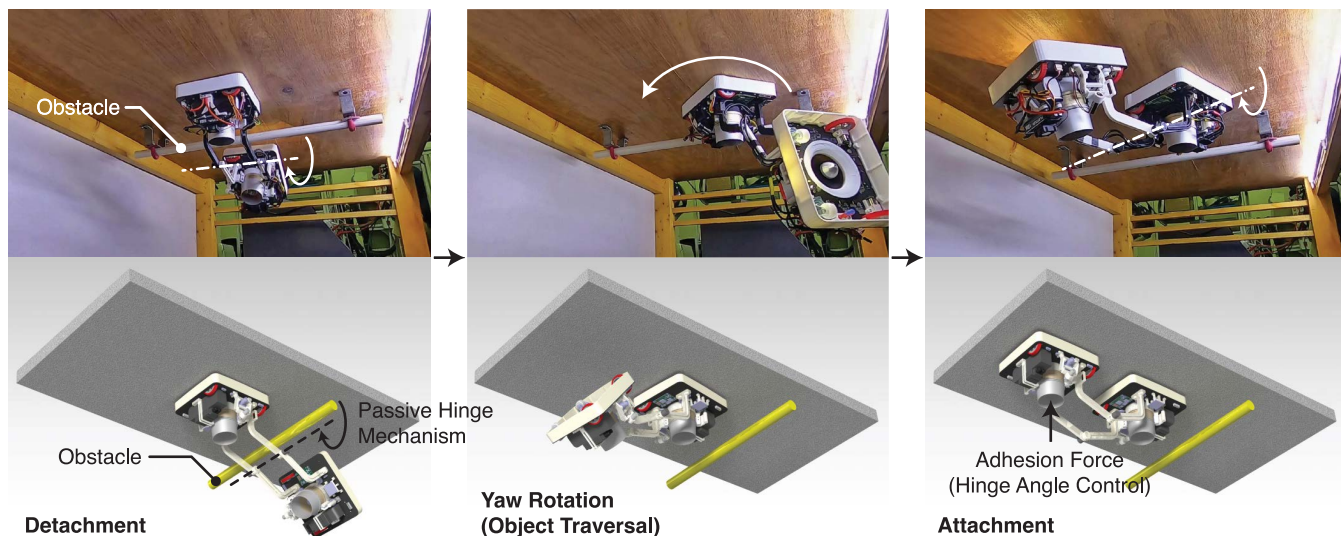
FIGURE 1. Obstacle traversal of the proposed robot system under kinodynamic constraints.

precise movement and imaging capabilities at short and fixed distances enable precise inspection of cracks on surfaces [8]. In addition, the robot's firm attachment capability enables teleoperation and manipulation using a robotic arm [9], [10] while robots are attached to the surface of operation. Therefore, climbing robots are more suitable than drones in such applications.

Various types of adhesion technologies have been developed to enable adhesion of robots to surfaces. These include suction cup adhesion, vacuum pump adhesion, magnetic adhesion, and bioinspired approaches that use nanotechnology-based materials [11], [12]. Among the different adhesion technologies for adhesion robots, a robot that applies magnetic adhesion can be firmly attached to steel surfaces [13]. The climbing robot proposed in a previous study [13] uses a magnetic crawler mechanism and can climb curved cylindrical surfaces with a payload of 75 kg. However, its applications are limited to tasks on specific metal surfaces. Robots that utilize a suction cup can be used independently of the material type; however, the surface properties, such as roughness, should be sufficient to generate suction because a decrease in the negative pressure within the suction cup due to air leakage causes adhesion failure. The climbing robot Sky Cleaner 3, which can clean a wall, was proposed in [14]; however, its surface material is limited to smooth glass walls. This is similar to a robot that uses a biomimetic approach, such as Stickybot [15], which is an experimental climbing robot that can climb vertical surfaces, such as glass, plastic, and ceramic tiles, at the speed of 4 cm/s. Although bioinspired adhesion methods and controls have been successfully implemented, they have not yet been applied to real-life scenarios because their adhesion is limited to smooth surfaces, and the presence of slight undulations and dirt may cause adhesion failure. A robot equipped with an electric ducted fan (EDF), such as the previously proposed vortex

climbing robot [16], uses the thrust generated by the EDF, which enables adhesion to any surface type. Simultaneously, the robot comprises wheels so that it can rapidly move along a surface while remaining attached to it. The adhesion of this vortex climbing robot was tested on several different types of surfaces with different curvatures, including the fuselage of a Boeing 737 and the interior of a water drainage pipe.

However, not all adhesion robots can traverse obstacles, which is a critical factor in performing feasible real-life tasks in different environments. For example, overhead piping or conduits attached to a ceiling obstruct the maneuver of robots, which are used by automated fire sprinkler systems to supply water in case of fire, as mandated by legislation in several regions globally. Other examples include ceilings that are often found in warehouses and buildings with suspended electrical wiring or piping as well as ceilings with a grid-shell structure that are framed, thus obstructing the locomotion of the robot. Although the aforementioned surfaces are generally limited to flat ceilings, obstructions are also present on curved surfaces, such as the dome structures of nuclear power plants and curved glass structures, including glass façades.

Therefore, an appropriate approach should be used for climbing robots to bypass obstacles and avoid obstructions during maneuvers. The climbing robots in [17] and [18] were developed to perform obstacle traversal as well as wall-to-wall climbing while using the magnetic adhesion method. In [17], the authors used velocity control of track wheels and torque feedback control of the active joint to ensure stable transition and obstacle traversal. The authors of [18] proposed a control method based on a dynamic model derived using Lagrangian formulation to perform stable locomotion by managing external forces. However, the robot uses magnetic adhesion, where the magnetic attachment

force cannot be fully controlled, and its methodology cannot be applied to non-metal surfaces. In addition, multi-joint robots with motorized hinges have been developed to traverse different obstacles and maneuvers in irregular environments while utilizing suction cup adhesion [19] or gripping mechanisms [20]. W-Climbot [19] performed a suction safety analysis to analyze the condition where the robot can be attached to the surface safely without slipping or falling during traversal or transition, but the analysis was limited to the quasistatic case. In addition, the robot was controlled by an operator via a joystick without a control system for locomotion. Similarly, Climbot in [20] was controlled manually by an operator, and safety analysis was not performed because the suction cup modules were replaced with the grasping module, and the chance of attachment failure was ignored. Additionally, their two-dimensional locomotion on surfaces is typically slow, owing to their unsuitability for use with wheels. In contrast, rapid movement can be achieved by a robot that uses an EDF and wheels to move around a surface without restriction of the surface material, but obstacles cannot be traversed in this manner [16]. Previous studies proposed the use of an aerial drone docked with a wall-climbing robot to avoid obstacles [21], [22]. Although these aerial drones may aid in the placement of a robot at the point of interest, the obstacle traversal capability of robots significantly improves inspection performance.

Therefore, this study developed a dual-unit climbing robot that adhere to various types of surfaces while traversing an obstacle and can rapidly maneuver using wheels (Fig. 1). The robot comprises two identical units joined by a passive hinge mechanism. Based on this mechanism, the robot can traverse an obstacle by varying the angle between units, which is achieved by changing the hinge angle. The hinges were unmotorized, and the hinge angle was controlled using a preexisting EDF, which generated thrust and adhesion forces. In contrast to motorized hinges, the use of unmotorized passive hinges not only reduces the weight of the robot by removing the motor from the hinge, but also reduces the moment applied to the robot unit that supports the detached unit, thus decreasing the probability of the unit rolling over, which would lead to attachment failure. The concept of using a hinge and two wall-climbing units with an EDF was previously proposed [23]. However, such a robot has never been developed and remains at the conceptual stage. Thus, its control mechanism is yet to be examined. In addition, the use of an actuated hinge with a motor and gearbox is proposed in the aforementioned concept, which increases both the total weight of the system and the moment applied to the attached unit.

In addition to the hardware and dynamic modeling of the robot, this study focused on the analysis of slipping and rollover conditions when a unit detaches from the attached surface. These analyses were considered while developing the control algorithm to prevent adhesion failure, not only during quasistatic movement, but also in more dynamic scenarios.

Previous research on robots with object traversal capability focused primarily on quasistatic movement without considering dynamics [17]. Static and dynamic analyses of robots have been conducted in previous studies, particularly for robots with a magnetic adhesion mechanism [18]. However, the authors in [18] did not apply these analyses to the control algorithm, and the robot was assumed to be slow such that it would not fall or slip during movements without any kinodynamic constraints. Generally, the class of problems in which kinematic and dynamic constraints are simultaneously satisfied [24] is referred to as "kinodynamics." This study focused on kinematic constraints, including traversing obstacles, and dynamic constraints, including the force or moment applied to the attached robot unit, while the other unit is detached from the surface.

In summary, this study proposed the design, modeling, and development of a unique dual-unit adhesion robot. In addition, dynamic analysis, as well as slipping and rollover condition analyses, were conducted when one of the units detached from the attached surface. Finally, three experiments were conducted to verify the proposed method. First, an EDF control test was performed to evaluate the adhesion force control (AFC) algorithm. The thrust produced by the EDF was measured and calibrated to ensure the accuracy of the AFC algorithm. Following calibration, the AFC algorithm was verified by controlling a single robot unit using a step response test, and the results were compared with the simulation results. Second, a maneuverability test of the adhesion robot was conducted on a curved surface. The scope of this test was not limited to verifying the maneuverability of the robot on the attached surface, but also extended to the comparison of the simulation results of the slipping condition analysis with those obtained from real-life experiments. Third, an obstacle traversal test was performed under kinodynamic constraints. Although the focus of the experiment was to assess the robot's traversal of an obstacle mounted on a ceiling, its actual purpose was to evaluate the proposed dynamics and control algorithms. Therefore, physical properties, such as the rate of change of the hinge angle and the critical force needed to prevent slipping or rollover, were analyzed thoroughly and compared with the simulation results. Subsequently, application scenarios to perform feasible real-life tasks using a system with obstacle traversal capability were considered in this study.

The main contributions of this study are as follows:
1) *Hardware design of robot*: A unique dual-unit adhesion robot that uses AFC and a passive hinge mechanism to traverse obstacles was developed, reducing both the weight and probability of adhesion failure.
2) *Modeling and analyses*: A dynamic analysis, as well as slipping and rollover condition analyses of the adhesion robot, were performed.
3) *AFC*: A control method that controls passive hinges based on dynamic analysis under the aforementioned kinodynamic constraints was established.

4) *Simulation and experiments*: Constraint analysis and a test of the control method to prevent adhesion failure were systematically performed, and the results were experimentally verified.
5) *Application scenarios*: Feasibility tests were conducted considering the proposed applications, and the results indicated the actual future applications of the system.

The remainder of this paper is organized as follows. Section II introduces the design of the robot, including the hardware diagram, EDF, and passive hinge mechanism. Driving modeling using differential kinematics, EDF control, dynamic modeling, and conditions to prevent the slipping or rollover of a robot are detailed in Section III. The experiments conducted to verify the feasibility of the proposed system as well as the dynamics and analyses presented in the previous section are discussed in Section IV. In Section V, several real-life application scenarios for the proposed system in various environments are presented to highlight potential future applications. Conclusions and final remarks are provided in Section VI.

II. PROPOSED SYSTEM

A. ROBOT CONCEPT
A climbing robot system that satisfies the following requirements and capabilities was proposed: precise scanning and inspection of attached surfaces, cleaning or maintenance work, and obstacle traversal to avoid or overcome obstacles present on surfaces. To achieve all these requirements, robot system hardware as well as versatile and robust control algorithms must be developed. Conventional drones do not satisfy these requirements, because precise movement is not feasible owing to their hovering characteristics. Moreover, conventional climbing robots struggle to traverse obstacles on surfaces because they must be completely detached while maintaining their balance. Thus, a new robot system must be designed to meet all the aforementioned requirements.

The proposed robot system (Fig. 2, 3, and 4) constitutes two identically shaped and sized units connected by a passive hinge mechanism (Section II-C). Each unit is equipped with an EDF and an electronic speed controller (ESC) for generating thrust and adhesion forces. Power was supplied by a lithium–polymer (LiPo) battery in each unit. Each unit was also equipped with an inertial measurement unit (IMU) for pose measurements. For the control unit, each unit contained a dedicated microcontroller unit (MCU) for actuation; whereas a selected unit was equipped with a single-board computer (SBC) to act as the host. However, the capabilities of both units were identical regardless of which one was the host. The SBC ran ROS 2 on the Ubuntu operating system and communicated with the MCUs of each unit to control the robot. The robot specifications are listed in Table 1. Certain peripherals such as load cells and bottom-facing cameras were not used in this study.

TABLE 1. Specifications of robot.

Parameters	Values
Dimensions (L × W × H)	175 mm × 510 mm × 165 mm (175 mm × 200 mm × 165 mm for each unit excluding arms)
Mass	2.68 kg (1.34 kg for each unit)
Power source	2 × 22.2 V, 2.8 Ah LiPo battery
Adhesion force	2 × ⌀70 mm EDF (at 22.2 V)
Processors	2 × MCU (STM32), SBC (Raspberry Pi with Ubuntu 20.04 LTS for ROS 2)
Wheel actuation	4 × DC motors with gearbox (ratio of 379:1)
Sensors	2 × IMU, 8 × load cell (0–5 kgf), 2 × hinge encoder, 2 × bottom-, 2 × front-facing camera (FHD, 30 fps), 2 × line laser (650 nm, 5 mW)
Communication	Wi-Fi, RF (with ground station)
Key performances	Max. adhesion force: 73 N, Max. speed: 0.25 m/s, Max. height of obstacle to traverse: 140 mm

(a)

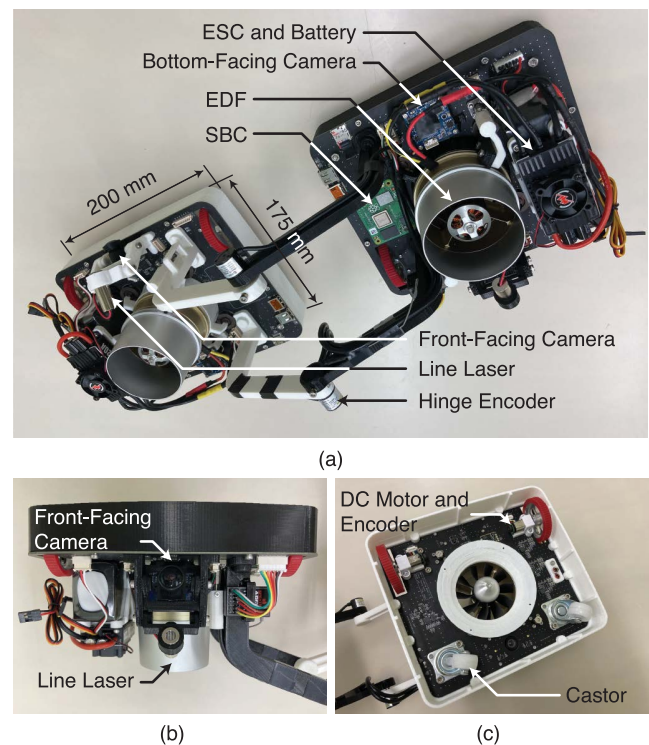(b)   (c)

FIGURE 2. Robot with two units connected by passive hinge mechanism: (a) overall view, (b) sensing system, and (c) driving system.

B. ADHESION METHOD
The robot was equipped with two EDFs, one in each unit, to generate thrust and perform AFC. A previous study reported that the gap between a ducted fan shroud and the surface affects the adhesion force. It was also revealed that an increase in the gap significantly reduces the negative pressure distribution [25]. Therefore, a plastic skirt was attached along the perimeter of each unit to increase the adhesion force. The experimental results demonstrate that the fan generated the maximum thrust of 21 N in mid-air, while the maximum sum
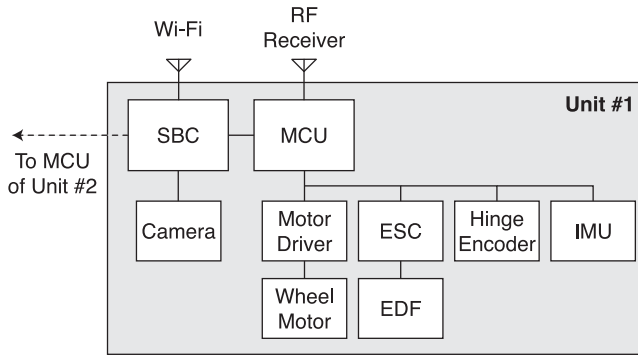
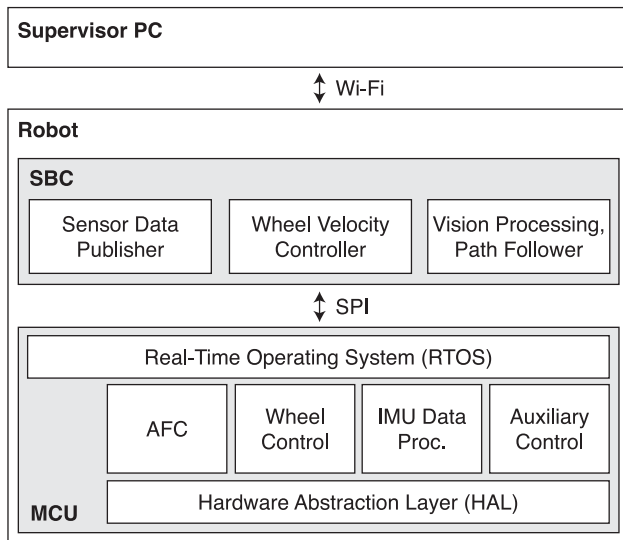**FIGURE 3.** Schematic of hardware configuration of robot.

FIGURE 4. Schematic of system configuration of robot.

of the adhesion force and the thrust was 73 N when the robot was attached to the surface.

C. PASSIVE HINGE MECHANISM

Unlike other climbing robots that employ motorized hinges to change the angle between hinges, the proposed robot utilizes a passive hinge mechanism comprising an absolute encoder to measure the hinge angle. Without using actuators such as motors in the hinges, the thrust generated by the EDF on each unit is used to rotate the hinged arms, thus enabling control of the angle between the two units. Therefore, the additional weight on the robot is reduced by removing the active components from the hinges, which is advantageous because of the increased payload and working time of the adhesion robot. In addition, the passive hinge reduces the moment and force exerted directly from the detaching unit on the attached unit that supports the entire robot, thereby decreasing the probability of rollover and attachment failure of the system.

In the proposed passive hinge mechanism, the angle between the hinged arms of each unit was measured using absolute encoders, one in each unit, which were located at the rotation axis of the hinged arms. The range of the hinge angle

that is constrained by the physical dimensions of the robot is between $-35°$ and $192°$ when defining the hinge angle as $0°$, while the two robot units are in contact with an identical flat surface. For the simulations described in Sections III-E and III-F, this range of hinge angle was narrowed from $0°$ to $180°$. This is because the minimum hinge angle while the robot is attached to the flat surface is $0°$, and the hinge angle is restricted to the maximum of $180°$ as a safety margin to avoid collisions between the two units.

In the proposed configuration, two units were connected using two pairs of passive hinged arms to traverse obstacles up to the height of 140 mm (Fig. 2), which was limited because of the physical dimensions of the hinged arms of the robot. If the targeted environment contains obstacles with heights greater than this limit, the robot may select a path containing only the traversable obstacle, as discussed in Section V. Moreover, if the robot is to be deployed in environments with only high obstacles, the hinged arms can be elongated to traverse such obstacles prior to deployment.

Although this passive hinge mechanism is advantageous owing to its lightweight characteristics and lower chance of adhesion failure by reducing the moment and force exerted on the attached unit, it has not been widely adopted for climbing robots. This is because, unlike the developed system that uses AFC to change the pose of the robot, a climbing robot that uses different adhesion technologies, such as magnetic adhesion or suction cup adhesion, cannot change the pose of the robot once the robot is detached from the attachment surface. Therefore, these adhesion robots typically should be equipped with motorized hinges, thus increasing the weight and decreasing the payload.

III. MODELING AND DESIGN

A. DRIVING CONFIGURATION

Each robot unit was equipped with wheels to enable free maneuverability around the attached surface and different driving configurations were possible. Several driving configurations can be applied to a robot, such as the Ackermann steering geometry. However, the steering mechanism occupies space and increases the overall weight of the system. In addition, precise alignment is required by such a steering geometry with a separate steering mechanism to achieve straight driving, which may be difficult to implement in small robots.

Therefore, owing to the size and weight constraints, and to achieve good steering precision, the configuration options were limited to differential steering, where the steering was performed by applying different torques to each wheel without adding any steering mechanism or actuators. Therefore, the feasible driving configurations included front-, rear-, diagonal-, and four-wheel driving (Fig. 5).

Unlike in the Ackermann steering geometry, lateral slip is inevitable if all the wheels are not aligned to be rotated along the same axis. However, smooth steering is impeded by this lateral slip and should therefore be minimized. Hence, a robot
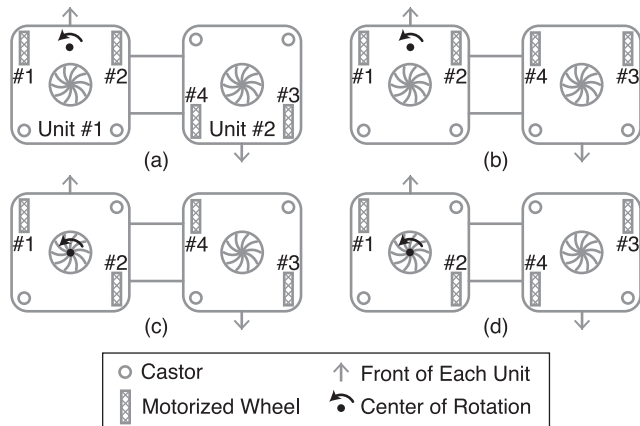
FIGURE 5. Different wheel configurations of robot.

TABLE 2. Symmetricity (Sym.) and lateral slip under different driving configurations.

Case	Driving	Sym.	$|\sigma|$			
			#1	#2	#3	#4
(a)	Front, front	Yes	0	0	0.276	0.501
(b)	Front, rear	No	0	0	0	0
(c)	Diag., diag.	Yes	0.615	0.615	0.138	0.251
(d)	Diag., diag.	No	0.615	0.615	0.251	0.138

configuration with two four-wheel-driven units is not ideal considering the lateral slip. Here, the lateral slip σ is defined as a term of the slip angle α (1), assuming that the robot maneuvers on a flat surface and that the camber angle is zero. v_x and v_y are the lateral and longitudinal velocity vectors, respectively, of the robot [26].

$$\sigma = \tan \alpha = -\frac{v_y}{v_x} \qquad (1)$$

Table 2 lists σ values of each wheel for each wheel configuration of the robot (Fig. 5). This lateral slip and the corresponding v_x and v_y were calculated assuming that the robot performed pure rotation around the center of rotation.

When only the slip component of each wheel in the lateral direction is considered, case (b) is the best choice because σ is zero for all the wheels. However, in this case, the robot is not point-symmetric to the center; therefore, friction may be insufficient when the robot climbs upward owing to the reduced normal force. In addition, the shapes of the robot units vary, and should therefore be designed differently. The next best choice is case (a), where lateral slip occurs only on the two wheels. In addition, the robot is symmetrical and each unit can be identical in shape, which is preferable. Therefore, the driving configuration in case (a) was chosen.

For this driving configuration, the motors attached to the wheel must produce sufficient torque to ensure that the robot can maneuver even if it is firmly attached to a wall by its EDFs. Therefore, a gearbox with the gear ratio of 379:1 was attached to each DC motor to produce sufficient torque, while
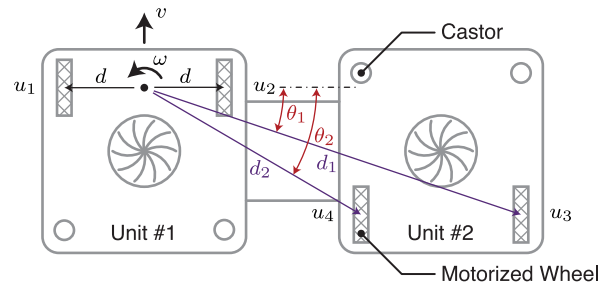

FIGURE 6. Driving modeling for wheels of each unit (top view).

a shaft-attached magnetic encoder measured the rotation of the motor shaft for the precise maneuvering of the robot.

B. DRIVING MODELING
Each robot unit was equipped with two actuated motors with an encoder; thus, the four wheels were appropriately controlled to move the two units as a single robot. Because there is no intersection between the centers of the turning circles of the two wheels on each unit, when following the path along a curve, tire slip is unavoidable, as discussed in Section III-A.

Therefore, the rotational speeds of all the tires u_1, u_2, u_3, and u_4 (Fig. 6), were calculated using (2) based on differential kinematics to drive the robot at linear and angular velocities of v and ω, respectively; r_w denotes the radius of each wheel, and the forward slips of wheels 3 and 4 were ignored during rotation because the friction coefficient in the side-slip direction exceeded that in the forward slip direction.

$$r_w u_1 = v - d\omega \qquad r_w u_3 = v + d_1 \omega / \cos \theta_1$$
$$r_w u_2 = v + d\omega \qquad r_w u_4 = v + d_2 \omega / \cos \theta_2 \qquad (2)$$

In addition, to achieve precise locomotion, a proportional-integral control algorithm is employed to control the rotation of the wheels. The control input for the rotational speed of the motor was measured using an encoder attached to it. The output signal was sent as a pulse-width modulated (PWM) signal to the motor driver in each unit.

C. ADHESION FORCE CONTROL
The AFC of the EDF was performed to adjust the hinge angle θ_h between the units using an algorithm that incorporated a proportional-derivative (PD) control feedback loop along with a feedforward loop to ignore the nonlinear gravitational term (Fig. 7). The effect of gravity exerted on the robot was eliminated by the feedforward torque, τ_g. The algorithm was executed in the MCU of each unit to separately control each EDF at the control period of 8.5 ms. The control input for the desired hinge angle, $\theta_{h,ref}$, was provided by the ROS 2 package running on the SBC.

The torque applied to the system $G(s)$ was calculated using the PD controller, which was converted to the EDF thrust and transmitted to the ESC. The output θ_h was measured using an absolute hinge encoder.
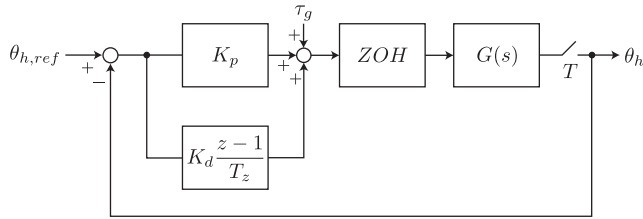
FIGURE 7. PD controller with feedforward loop for gravity compensation.
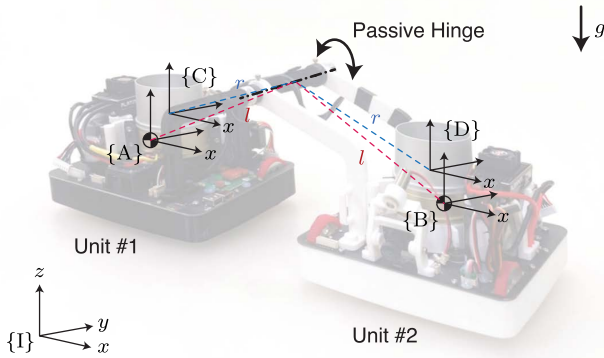

FIGURE 8. Coordinate frames of robot system.

D. DYNAMIC MODELING

The dynamic modeling of the robot system was established for the design of the control algorithm of the robot and to analyze the kinodynamic constraints of the slipping and rollover conditions, which is one of the main contributions of this study. The robot system was modeled as a two-link manipulator because of the passive hinge mechanism linking its two units. In this configuration, a unit ("the first unit") is attached to a wall, while the other unit ("the second unit") can freely detach from the wall to perform various tasks, such as obstacle traversal. However, it is challenging to maintain adhesion of the first unit when the second unit detaches from the wall and rotates aggressively.

Therefore, the first unit should remain attached to the surface despite exertion of an external wrench from the second unit. This external wrench is generated by forces, including inertial force and thrust from the EDF of the second unit, which may cause the robot to slip or even roll over. Therefore, a precise analysis of robot dynamics must be conducted to solve these challenges by considering the kinodynamic constraints for the safe and stable control of the system.

First, the coordinates of the system were defined (Fig. 8). The body frames of the first and second units are denoted by {A} and {B}, respectively, and the thruster body frames of the first and second units are denoted by {C} and {D}, respectively. The inertial frame of the system is denoted as {I}. The length of the virtual arm between the rotation axis of the passive hinge and the center of mass of each unit is represented as l, and the distance between the hinge and the thruster is denoted as r.

To analyze the dynamics of the system, modeling was performed using the Newton–Euler formulation, which is extensively used for modeling robot arms or aerial manipulators that interact with the external environment [27], [28], similar to our case. Assuming that the robot is rigid, the expression can be derived using a twist–wrench formulation, as indicated by (3). $\mathcal{G}_b$ is the spatial inertia matrix of the body, which is composed of the inertia matrix $\mathcal{I}_b$ and body mass m, multiplied by a 3×3 identity matrix $I_{3\times3}$. The generalized wrench exerted on the body is denoted by $\mathcal{F}_b$; whereas the twist and its derivative of the rigid body in the body frame are represented as $\mathcal{V}_b$ and $\dot{\mathcal{V}}_b$, respectively. Finally, the definition of the Lie bracket $[\text{ad}_\mathcal{V}]$ of $\mathcal{V} = (\omega, v)$ is expressed in (5), where $[\cdot]_\times$ is the skew-symmetric operator of the matrix.

$$\mathcal{F}_b = \mathcal{G}_b \dot{\mathcal{V}}_b - [\text{ad}_{\mathcal{V}_b}]^\mathsf{T} \mathcal{G}_b \mathcal{V}_b, \quad (3)$$

$$\text{where } \mathcal{G}_b = \begin{bmatrix} \mathcal{I}_b & 0_{3\times3} \\ 0_{3\times3} & mI_{3\times3} \end{bmatrix} \in \mathbb{R}^{6\times6}, \quad (4)$$

$$\text{and } [\text{ad}_\mathcal{V}] = \begin{bmatrix} [\omega]_\times & 0_{3\times3} \\ [v]_\times & [\omega]_\times \end{bmatrix} \in \mathbb{R}^{6\times6}. \quad (5)$$

Equation (3) can be expressed in the form of (6) as follows:

$$M(q)\ddot{q} + C(q, \dot{q})\dot{q} + G(q) = J_c^\mathsf{T} \mathcal{F}_{ext}, \quad (6)$$

where q denotes the generalized coordinates of the model. The inertial matrix, Coriolis and centrifugal terms, gravitational torque vector, and input wrench vector are denoted as M, C, G, and $\mathcal{F}_{ext}$, respectively. The Jacobian for the thruster location with respect to the passive-hinge rotation axis is represented by J_c.

During the backward wrench calculations from the end-effector frame to the global frame, the external wrench exerted on the end-effector must be determined. However, because the centers of gravity of the second unit and thruster are different, the wrench generated by the thruster in {D}, $\mathcal{F}_D$, must first be converted to the end-effector frame of {B}. This conversion can be performed using an adjoint representation of the transformation matrix. Based on its definition, the representation $[\text{Ad}_{T_{DB}}]$ of the matrix, $T_{DB} = (R_{DB}, p_{DB}) \in SE(3)$, can be expressed as follows:

$$[\text{Ad}_{T_{DB}}] = \begin{bmatrix} R_{DB} & 0_{3\times3} \\ [p_{DB}]_\times R_{DB} & R_{DB} \end{bmatrix} \in \mathbb{R}^{6\times6}, \quad (7)$$

where the rotation matrix R_{DB} is a representation of the orientation of frame {B} in {D}, and the vector $p_{DB} \in \mathbb{R}^3$ represents the origin of {B} in {D}. The conversion of the wrench from {D} to {B} can be expressed by (8), as follows:

$$\mathcal{F}_B = [\text{Ad}_{T_{DB}}]^\mathsf{T} \mathcal{F}_D. \quad (8)$$

Using the Newton–Euler formulation, the wrench exerted on the first unit when the second unit rotates can be calculated. This allows the analysis of slipping and rollover conditions, which is one of the main contributions of this study owing to its significance in ensuring the stable operation of the robot system without experiencing

adhesion failure. The analyses are presented in detail in Sections III-E and III-F.

E. SLIPPING CONDITION ANALYSIS

For a robot to traverse an obstacle, the first unit must be rigidly attached to the surface of interest using thrust to prevent slipping or rolling over. Such slipping or rollover may be caused by the force or moment exerted by the second unit on the first unit attached to the surface when the second unit detaches from the surface. Previous studies on robots with object traversal capability have focused mainly on quasistatic movement without considering dynamics. In addition, studies that investigated the statics and dynamics of robots did not apply these analyses to the control algorithm; thus falls or slips were ignored during movement. Therefore, one of the main contributions of this study is the investigation of the slipping and rollover conditions to prevent adhesion failure.

In this section, the slipping condition of the robot is analyzed when external forces are exerted on the first unit; the rollover condition induced by the moment is presented in Section III-F. The analyses were performed for the following two scenarios: (1) the worst-case scenario, where the second unit loses control and free-falls, and (2) the controlled scenario, where the unit is controlled by the algorithm described in Section III-C.

Simulations were conducted using a customized MATLAB simulator based on the equations of motion derived in Section III-D. The objective was to analyze the wrench exerted on the first unit when the second unit free fell at different angles of the surface by varying the roll and pitch of the robot from −180° to 180° in increments of 5°. The Runge–Kutta fourth-order integrator was used for the simulation period of 5 s with the timestep of 8.5 ms, and free-falling of the second unit owing to gravitational force was observed. The simulation range of θ_h was restricted between 0° and −180° to ignore the conditions in which rotation (free fall) does not occur, such as when the robot is on the ground or when the two units collide. Initially, the two units were attached parallel to a flat surface at $\theta_h = 0°$. The pose of the robot system was simulated as the rotation of the inertial frame, assuming that the robot was fixed to the ground. For example, the gravity vector pointed upward in a snapshot of the simulations (Fig. 9), suggesting that the first unit was attached to an 180°-rotated ceiling.

The wrench pair of the force and moment exerted on the robot can be determined using the Newton–Euler formulation. Moreover, the critical force required to prevent the unit from slipping is given by F_s, which is the minimum adhesive force on the first unit required in the −z-direction of {A}. F_s can be calculated from (9), where F_z and $F_{xy} = (F_x^2 + F_y^2)^{1/2}$ are the z-directional and xy-plane force components from the wrench exerted on the first unit in frame {A}, respectively. The static coefficient of friction between the rubber wheel and wooden surface is denoted as μ_s, and its value was experimentally determined to be 0.55.

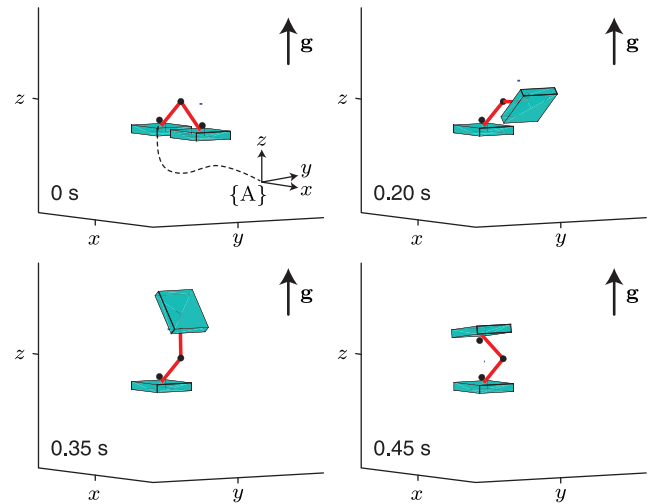$$F_s = \max(F_z + F_{xy}/\mu_s) \qquad (9)$$

FIGURE 9. Simulation of free fall using customized MATLAB simulator.

However, based on the results of the slipping simulations, it is inferred that this is impossible because F_s is larger than the maximum force generated by the duct (red surface in Fig. 10a). There is a sharp drop in F_s at a particular pitch angle because the robot starts to free-fall at these critical points where a unit starts to detach from the attached surface.

Therefore, the simulations were repeated while the second unit was controlled using the algorithm described in Section III-C to verify whether the algorithm prevented the robot from slipping. The initial and final θ_h were set to 0° and −90°, respectively, to traverse an obstacle. The detachment rate was set to 0.4 rad/s, which was the same as the experimental value discussed in Section IV-C. For the same reason, K_p and K_d were 3.0 and 0.5, respectively. The F_s value was decreased for all roll and pitch angles by the control algorithm under the maximum force that the duct can generate (Fig. 10b), thereby confirming that the control method can inhibit the slipping of the robot at different surface angles.

F. ROLLOVER CONDITION ANALYSIS

As a continuation of our study indicated in the previous section, the rollover condition for the robot system was analyzed and presented in this section. A unique method that models the unit of a climbing robot as a cylinder was devised to simplify the calculations and simulations of a rollover condition. In this method, the first unit was modeled as a right circular cylinder with its base on the adhesion surface, which could be rolled over owing to an external moment. This is similar to a water bottle that tips under external torque. Subsequently, a coordinate system was established for the analysis (Fig. 11).

In Fig. 11, the frames attached to the center and perimeter of the base are denoted as {E} and {F}, respectively. In each frame, the x-axis is denoted as x and the z-axis (not denoted) is the vertical vector pointing upright. The cylinder radius vector from the origin of {E} to the origin of {F} is denoted
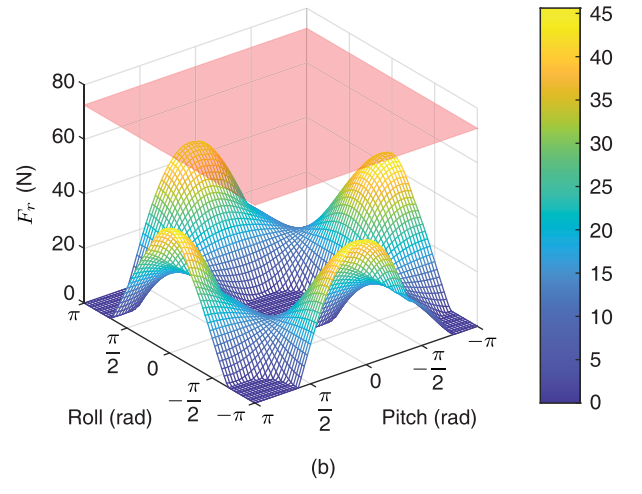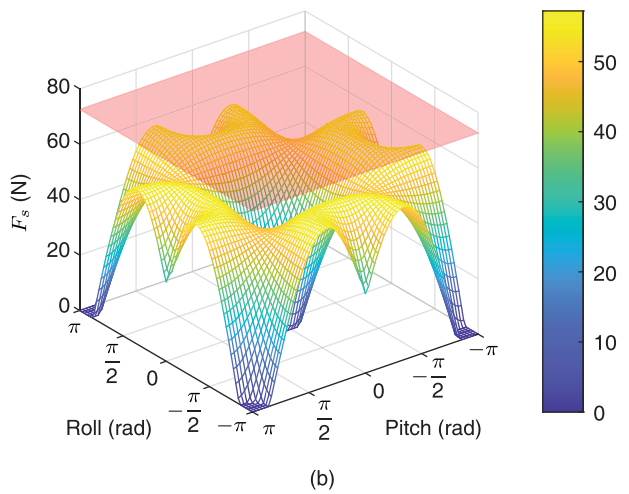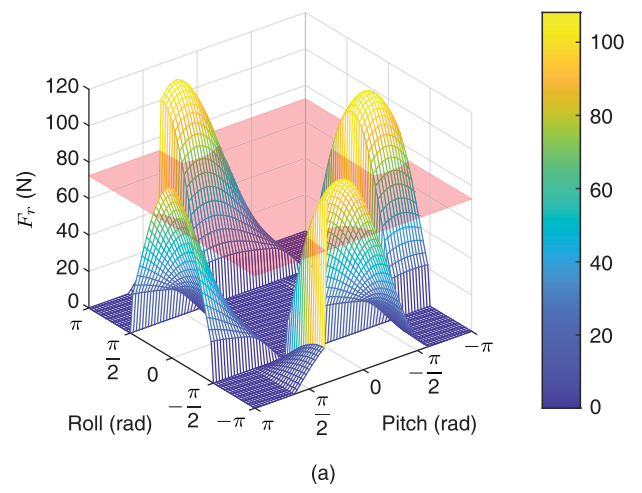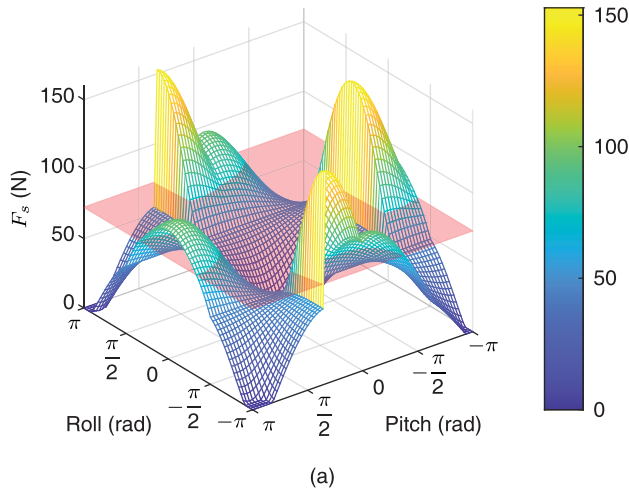
FIGURE 10. Simulation results of F_s to prevent robot from slipping during (a) free fall and (b) controlled detachment. Red plane denotes the maximum thrust force of the robot.

FIGURE 11. Rollover condition modeling of first unit.

by r_{cyl} with length r_{cyl}, and the angle between r_{cyl} and the x-axis of {E} is denoted by θ_{cyl}. The force and moment exerted on the center of the first unit expressed in the frame of {E} are denoted by $f_E \in \mathbb{R}^3$ and $m_E \in \mathbb{R}^3$, respectively. Here, the x-axis of {F} was aligned with that of $\mathbf{r}_{cyl}$. The transformation matrix between frames {E} and {F} is represented by the T_{EF}, which is expressed as (10) and consists of a rotation matrix

FIGURE 12. Simulations of F_r to prevent robot from rolling over during (a) free fall and (b) controlled detachment. Red plane denotes the maximum thrust force of the robot.
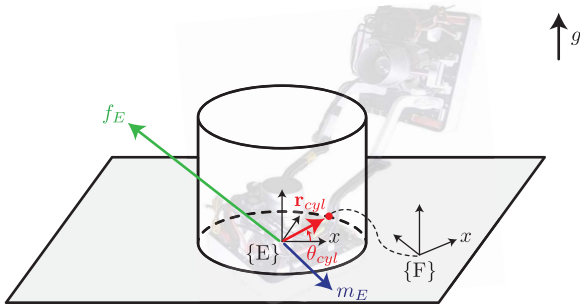
with respect to the z-axis and vector r_{cyl}.

$$T_{EF} = \begin{bmatrix} \cos\theta_{cyl} & -\sin\theta_{cyl} & 0 & r_{cyl}\cos\theta_{cyl} \\ \sin\theta_{cyl} & \cos\theta_{cyl} & 0 & r_{cyl}\sin\theta_{cyl} \\ 0 & 0 & 1 & 0 \\ 0 & 0 & 0 & 1 \end{bmatrix} \in SE(3) \quad (10)$$

The angle θ_{cyl} at which rollover occurs is currently unknown. However, by thoroughly observing frame {F}, it can be concluded that the positive net moment in the y-direction of frame {F} causes the cylinder to roll over. Because the wrench pair exerted on the center of the first unit {E} is known as $\mathcal{F}_E$, using the Newton–Euler formulation, this wrench pair can be further translated to frame {F} as $\mathcal{F}_F$ to determine the moment on the y-axis of {F} using (11). The force and moment exerted on the first unit expressed in the $\mathcal{F}_F$ frame are denoted by $f_F \in \mathbb{R}^3$ and $m_F \in \mathbb{R}^3$, respectively.

$$\mathcal{F}_F = [\mathrm{Ad}_{T_{EF}}]^\mathsf{T}\mathcal{F}_E = \begin{bmatrix} m_F^\mathsf{T} & f_F^\mathsf{T} \end{bmatrix}^\mathsf{T} = \begin{bmatrix} m_F \\ f_F \end{bmatrix} \quad (11)$$

To obtain the unit vector in the y-direction of frame {F}, $\hat{\mathbf{y}}_F$, the cross-product of the two vectors, $\mathbf{r}_{cyl}$ and the z-directional

unit vector, was determined, and then divided by the size of $\mathbf{r}_{cyl}$.

$$\hat{\mathbf{y}}_F = \frac{[0\ 0\ 1]^\mathsf{T} \times \mathbf{r}_{cyl}}{r_{cyl}} \tag{12}$$

The dot product of $\hat{\mathbf{y}}_F$ and m_F yields the y-directional net moment, $M_{F,y}$.

$$M_{F,y} = \hat{\mathbf{y}}_F \cdot m_F \tag{13}$$

As indicated in the previous section, the thrust of the first unit should exceed the critical force to prevent the unit from rollover, F_r, as expressed in (14).

$$\Sigma M_y = M_{F,y} - r_{cyl}F_r < 0 \tag{14}$$

Equation (14) can be simplified as follows:

$$F_r > \frac{M_{F,y}}{r_{cyl}}. \tag{15}$$

At this point, the angle θ_{cyl} at which the rollover occurs must be determined. Therefore, similar to the simulations described in Section III-E, frame {F} was rotated by varying θ_{cyl} from 0° to 360° and the maximum F_r was calculated. θ_{cyl} with the maximum F_r is expected to be the point at which rollover occurs if the maximum possible thrust force of the EDF is smaller than F_r.

The simulation results demonstrate that the calculated F_r was larger than the maximum force at a particular roll and pitch of the attached surface (Fig. 12a). Thus, rollover may occur when the second unit free falls without an appropriate control algorithm, similar to the results discussed in Section III-E. A sharp decline in F_r was observed, as under the slipping condition, because these are critical points at which a unit starts to detach from the attached surface.

The simulations were repeated, as detailed in Section III-E, to verify whether the control algorithm applied to the second unit could prevent the robot from rolling. The control parameters were identical to those used in the simulations discussed in the previous section. The results indicate that F_r is smaller than the maximum adhesive force that the robot can generate at every surface angle (Fig. 12b). Therefore, the robot can be stopped from slipping and rolling over at any desired roll and pitch angle using an appropriate control algorithm. Furthermore, stable operations can be performed by the developed robot in any scenario.

IV. EXPERIMENT

A. EDF CONTROL TEST

Tests were performed to evaluate the AFC algorithm proposed in Section III-C, and the results were compared with the simulation results. For the tests, the first unit was attached to a 180°-rotated surface (ceiling) and the EDF of the free-hanging second unit was regulated using an algorithm to control θ_h. As indicated in Section II-B, the adhesive force increased as the gap between the adhesion surface and the EDF decreased. Therefore, to prevent this nonlinearity, the
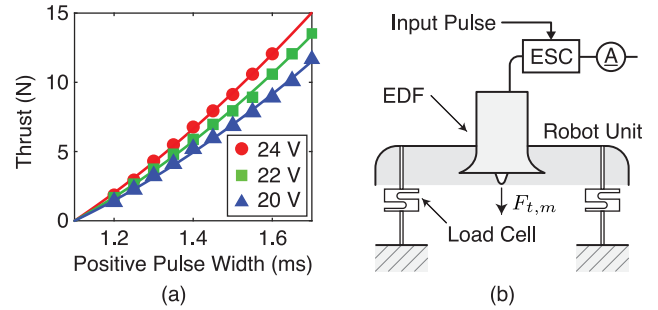

FIGURE 13. (a) EDF calibration results at different voltages and (b) settings for measuring EDF thrust.
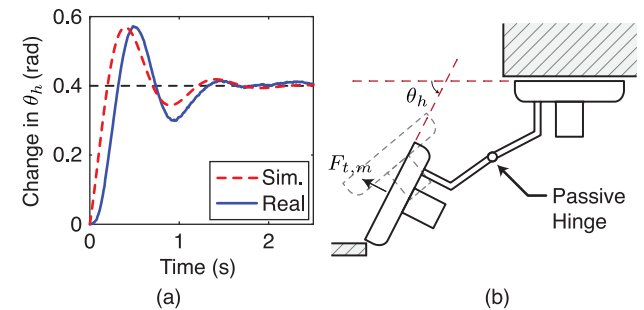

FIGURE 14. (a) Step response results and (b) settings for testing step response.

second unit was located far from any surface during the test and generated mid-air thrust from the EDF. In addition, a gravitational feedforward term τ_g, which is proportional to the value of $\cos\theta_h$, was added to ignore the effect of gravity during control, as discussed in Section III-C. Thus, the gravitational force can be ignored during control.

Prior to the control test, the correlation between the thrust generated by the EDF and the positive pulse width of the input PWM signal to the ESC was analyzed. This calibration process is necessary to achieve accurate thrust generation, primarily because errors in the calibration may lead to inaccurate gravitational compensation of the robot, which may affect the performance of the control system. The calibration was performed by attaching the EDF to the load cell and supplying different voltages to the ESC ranging from 19.2 V (3.2 V per cell) to 24.6 V (4.1 V per cell) in increments of 0.2 V (Fig. 13b). Subsequently, the correlations were fitted to the second-degree polynomial equations. The maximum thrust generated by the EDF was 21 N. Certain calibration results obtained at different voltages are displayed in Fig. 13a.

Following the calibration, the step responses of the EDF were tested. Fig. 14a shows one of the step responses with the step input of 0.4 rad, where the initial θ_h was –0.933 rad and the final θ_h was –0.533 rad. In this particular test, K_p and K_d were set to 2.5 and 0.25, respectively. The test results presented a response similar to that of the simulations, except for a slight lag in the response and small oscillations in the steady state. This difference may be attributed to the bending of the plastic-hinged arms, nonlinearity and hysteresis of the ESC, and inherent delay of the ESC. Nonetheless, from
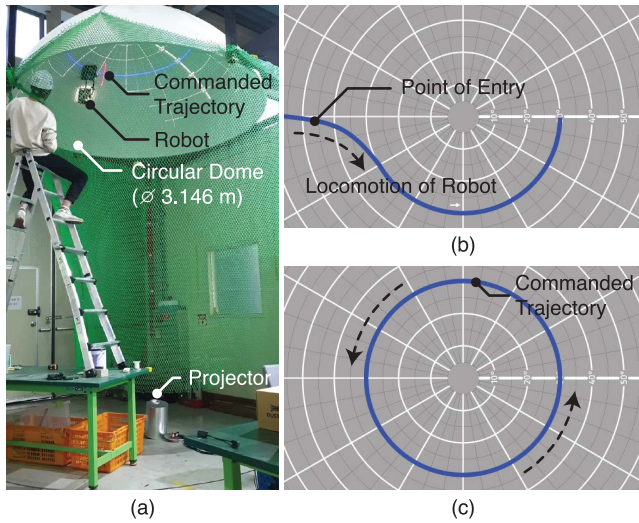
FIGURE 15. Maneuverability test on curved surface: (a) test settings, (b) projected pattern at start of maneuvering (with point of entry), and (c) projected pattern after the robot enters the circular trajectory.

FIGURE 16. Overlapped image of robot trajectory during maneuverability test on dome.

FIGURE 17. Attachment of proposed robot system on (a) accelerating car, (b) flat wall, and (c) 90°-angled wall.

the results, it can be inferred that the control algorithm compensates for the nonlinear gravitational term to behave like a linear system and that the robot can be assumed to be an ideal theoretical model.

B. MANEUVERABILITY TEST ON SURFACES

A feasibility test was performed to verify the slipping condition of the robot and its maneuverability on the attached ceiling. Because the maneuvering of a robot on a curved surface is more difficult than that on a flat surface, it was tested on the curved surface of a spherical dome (Fig. 15a). The height of the dome was 1.1 m, the diameter of the base was 3.0 m, and the radius of the sphere was 1.573 m. The first unit was driven along a circle with the polar angle of 30°, which positioned the second unit at the polar angle of 43.5° owing to the length of the robot. Based on the simulations, the critical forces required to prevent slipping and rollover of each unit were determined as 24.8 and 28.0 N when the robot unit was located at polar angles of 30° and 43.5°, respectively. Therefore, the robot units were operated with a safety margin of approximately 40% to generate attachment forces of 35 and 40 N, respectively.

The desired route was set by a laser projector mounted on the ground, after which the first robot visually tracked it using a front-facing camera to automatically perform the test without manual control. To test the maneuvering on a circular trajectory, as shown in Fig. 15b, the robot first entered through the point of entry, following the set projected route in blue. When the robot enters the circular path, the projected route changes to a circle (Fig. 15c); therefore, the robot can maneuver around a circular trajectory. A pure pursuit algorithm was used to follow the set route. During locomotion, the trajectory of the robot was observed using a wide-angle camera mounted at the center of the dome to
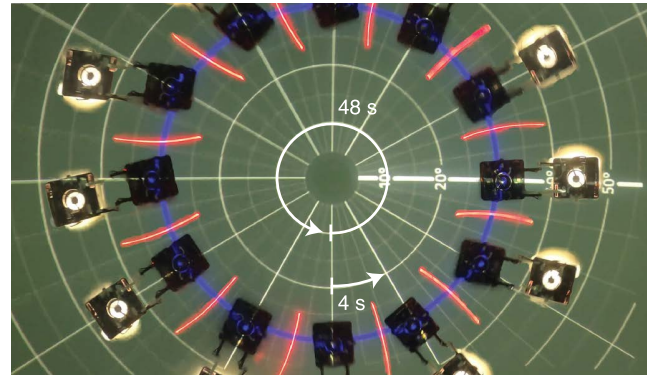
enable subsequent processing to calculate the deviation of the robot from a set route.

The trajectory of the robot demonstrated that the set route was followed by the first unit within the maximum angular deviation of 2°, equivalent to the linear deviation of 0.05 m (Fig. 16). In addition, the robot did not fall from the dome during the experiment because there was no loss of static friction, verifying the maneuverability of the robot, even on a curved surface. The experimental results verify the differential kinematics and control algorithms of the wheels, which are addressed in Section III-B.

In addition to the aforementioned test on the curved surface of the dome, a preliminary field test was conducted to qualitatively assess the feasibility of the robot on various surfaces (Fig. 17). The results demonstrate that the robot can even be attached firmly to the external surface of an accelerating car (Fig. 17a), and that vertical and horizontal movements are also possible on different types of surfaces (Fig. 17b and c), indicating the future industrial applicability of the system. Further application scenarios are presented in Section V.

C. OBSTACLE TRAVERSAL TEST

An experiment was performed to evaluate the developed dynamics and control algorithms. In this experiment, a case in which the robot partially traversed an obstacle was analyzed. To achieve this, a pipe was attached 80 mm from the ceiling, although this was not the maximum height that the robot could traverse. The experiment was executed based on the following profile comprising three consecutive control phases:
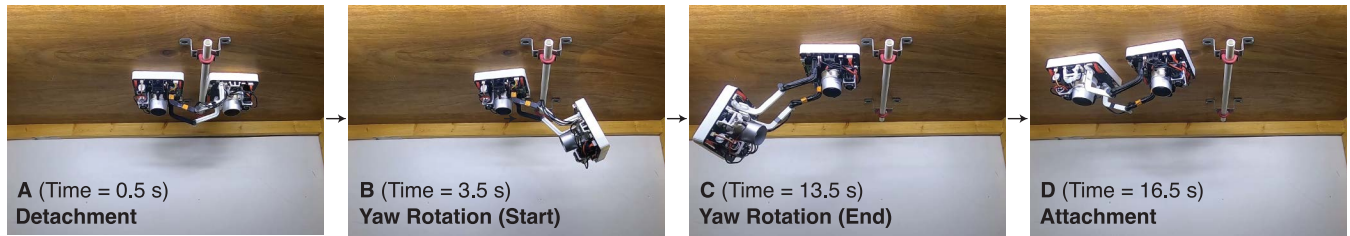
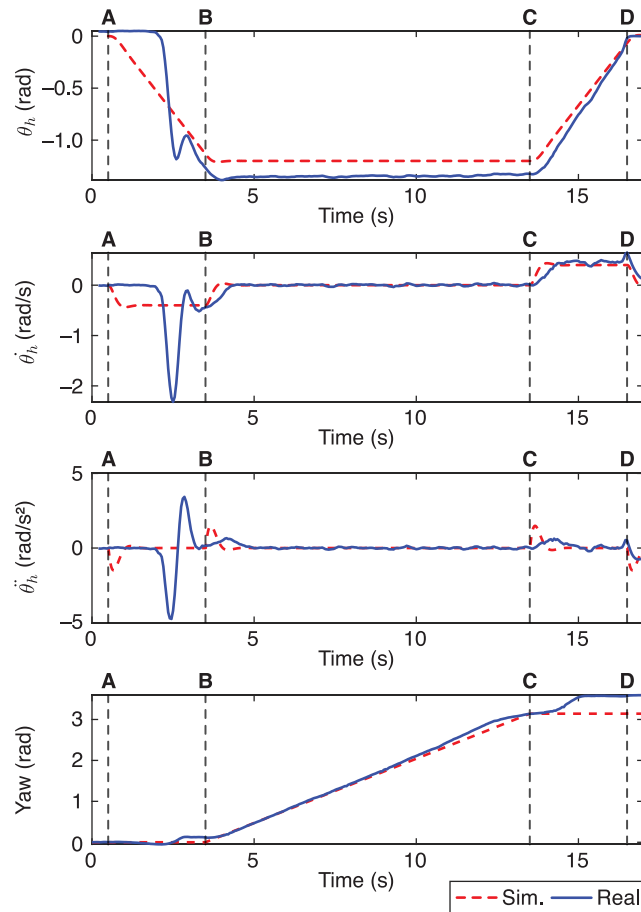**FIGURE 18.** Detachment, yaw rotation, and attachment of robot.

FIGURE 19. Simulation and experimental results of test on ceiling.

1) *Detachment*: θ_h was controlled using the PD control algorithm discussed in Section III-C, with $K_p = 3.0$ and $K_d = 0.5$. The hinge was proportionally lowered from 0 to −1.2 rad within 3 s.

2) *Yaw rotation*: The robot was rotated at the rate of 0.1π rad/s to complete a half revolution in 10 s using the wheel control algorithm described in Section III-B.

3) *Attachment*: The second unit was attached to the ceiling by increasing θ_h from −1.2 to 0 rad in 3 s, similar to the detachment phase. The control parameters remained unchanged.

The entire process was executed autonomously (Fig. 18 and 19), and the simulations were performed using MATLAB (Fig. 19). Although the second unit without the
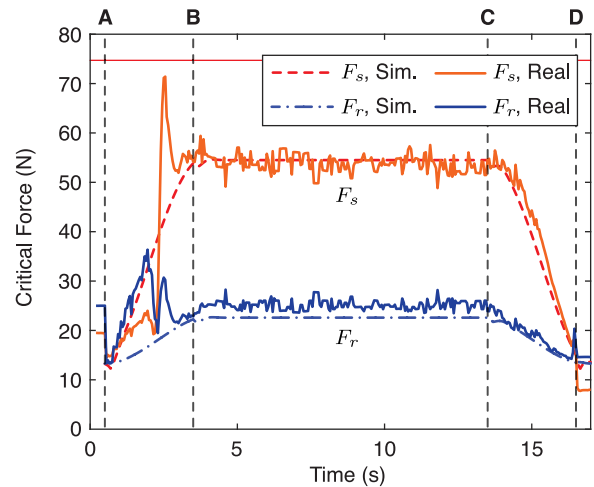

FIGURE 20. Calculated critical force to prevent slipping and rollover during experiment.

SBC was detached from the ceiling in this experiment, the capabilities of the two units were identical; thus, their roles could be switched. Note that another repetition of the process completes the full object traversal of both units. However, this study focused on the physical analysis of the half-traversal of the phases, as opposed to their application and mission completion.

Based on the experimental results (Fig. 18 and 19), the detachment phase was from A to B, ranging from 0.5 to 3.5 s, and the yaw rotation phase was from B to C, ranging from 3.5 to 13.5 s. Moreover, the attachment phase was from C to D, ranging from 13.5 to 16.5 s. The changes in the yaw angle from A to B, B to C, and C to D were 0.11 rad (6°), 3.02 rad (173°), and 0.44 rad (25°), respectively, which were measured using an IMU. The simulation and experimental results demonstrated similar tendencies, except for the sudden detachment and fall at 2–3 s and yaw rotation during the attachment at 14–16 s. The abrupt detachment was caused by the mid-air thrust being significantly smaller than the adhesive force when the robot was placed near the ceiling, as indicated in Section II-B. This is expected because air is a compressible fluid, and quantitative modeling is very difficult. Therefore, this nonlinear decrease in the adhesion force could not be adequately controlled using a PD-based controller. The yaw rotation during attachment can be attributed to the increased angular momentum
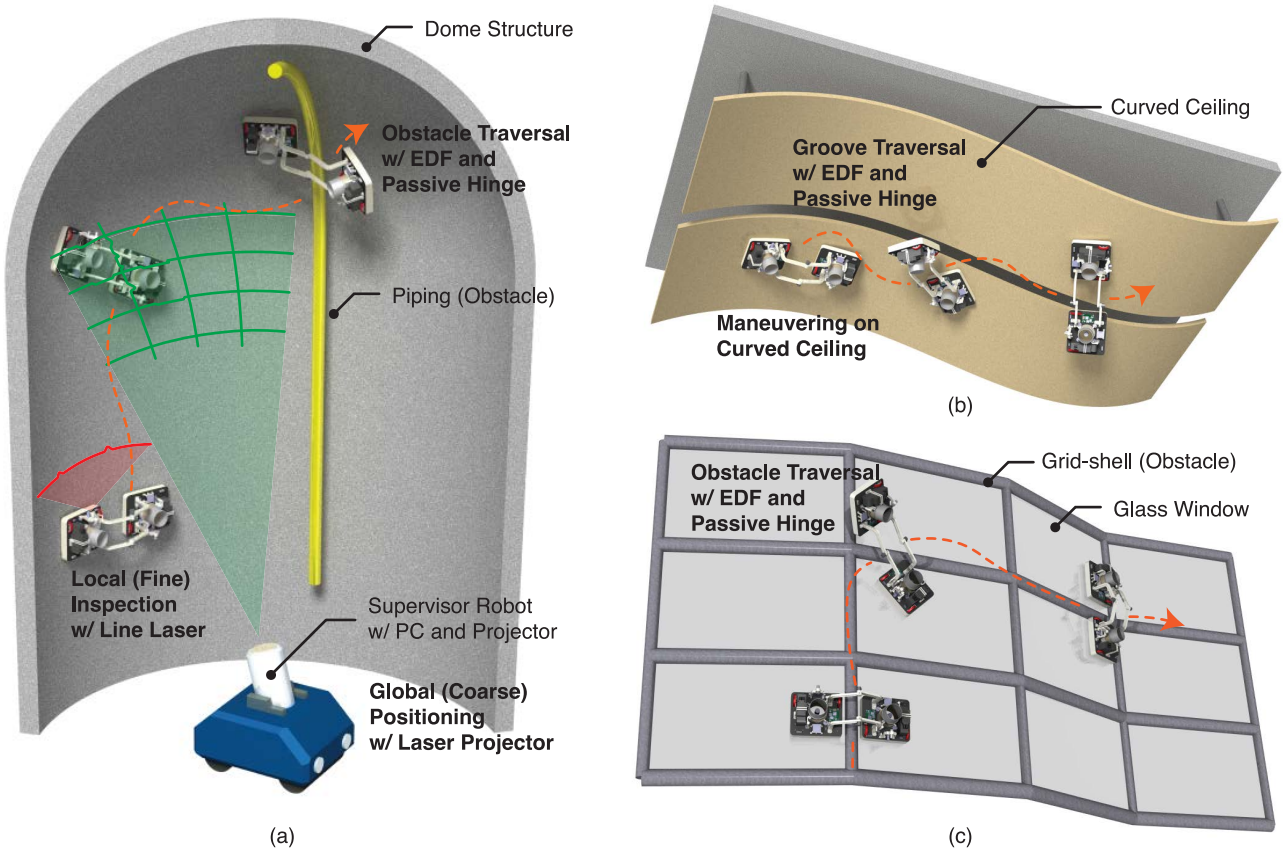
FIGURE 21. Application scenarios of proposed robot system: (a) dome structure with obstacle, (b) curved ceiling with gap, and (c) glass façade with a grid-shell structure.

generated by the EDFs, because they rotate in the same direction.

F_s and F_r, which are the critical forces for preventing slipping and rollover of the robot, respectively (as described in Sections III-E and III-F), were calculated based on the experimental results and compared with the values obtained via simulation (Fig. 20). The results indicate that F_s and F_r exhibited similar tendencies during the actual experiment to the simulation results. However, as previously indicated, the sudden detachment and fall at 2–3 s were observed to exert an abrupt force on the first unit and maximize F_s, thus causing slipping of the robot.

Apart from the inevitable sudden slip that occurred during the experiment, the effects of the proposed dynamics and control algorithm were shown to be feasible and consistent with the simulation results. Furthermore, this experiment demonstrated the feasibility of the robot to successfully traverse an obstacle using detachment, yaw rotation, and attachment in practical tasks.

V. APPLICATION

As indicated in Section IV-C, the robot can traverse an obstacle on the adhesion surface, and slipping and rollover can be prevented by the aforementioned AFC algorithm. This indicates that various applications of the developed system

are possible for real-life tasks in complex environments. Several applications are illustrated in Fig. 21.

The first application (Fig. 21a) on a dome structure was proposed based on a previous study [21] in which a wall-climbing robot, along with a supervisor robot on the ground equipped with a laser projector, projects a virtual landmark to interact with robots under the surface without distinctive features. In this scenario, a wall-climbing robot utilizes various mounted devices, such as a line laser or front-facing camera, to perform local (fine) localization and inspection of the attached surface, while the projected laser pattern from the supervisor robot acts as a virtual landmark and helps global (coarse) localization. In addition, such devices can help identify the height of each obstacle and distinguish the obstacles with the height that can be traversed by the configuration of the robot; thus, the robot can select the path that passes only obstacles with traversable height.

The second application (Fig. 21b) proposes the use of the developed system on ceilings, where a gap (groove) exists between the two inspection surfaces. Similar to the first scenario, the climbing robot can perform local inspection using a line laser and camera, while the entire process is supervised by a ground vehicle that projects a laser pattern to facilitate global localization. The robot can smoothly and rapidly maneuver along the curved surface owing to the four

motorized wheels, and the gap can be traversed using the passive hinge mechanism and AFC. Therefore, inspection can be continued by the robot on the other surface.

The third application (Fig. 21c) proposes the use of the system on grid-shell structures, such as glass façades, which are commonly found in architecture such as indoor shopping malls. The use of the proposed system on such structures is beneficial because the steel reinforcements that join glass panels obstruct the locomotion of conventional adhesion robots. In these structures, the obstacle traversal capability of the robot can help it easily traverse obstacles between the panels.

In summary, the proposed adhesion robot system has several advantages for the following reasons:

- Unlike conventional wheel-based adhesion robots, an obstacle on an adhesion surface can be easily traversed using the passive hinge mechanism of the proposed system.
- Owing to its EDF-based thrust generation, adhesion can be achieved on most surface materials, unlike an adhesion robot that uses magnetic adhesion or a biomimetic approach.
- Because the proposed system can be firmly attached to surfaces, unlike conventional drones, the inspection and teleoperation capabilities are significantly enhanced.
- The use of the projected pattern as a virtual landmark can greatly improve the inspection capability of the proposed system, which will be further studied in future work.

VI. CONCLUSION

In this study, a dual-unit adhesion robot powered by an EDF was designed, modeled, and analyzed. Specifically, the design of the robot system and its driving modeling using differential kinematics, control method of the EDF, and dynamic modeling of the system based on the Newton–Euler formulation were established. In addition, the slipping and rollover conditions of the robot when one of the units detached from the ceiling were analyzed and verified through practical tests and simulations using MATLAB.

The obstacle traversal experiment further verified that a suitable control algorithm of the EDF enables stable locomotion of the robot without slipping or rolling over from the ceiling, demonstrating its feasibility and effectiveness in real-life tasks. A feasibility test on a curved surface was conducted to verify the slipping condition of the robot and its maneuverability on an attached ceiling. Finally, real-life scenarios for the application of robots in complex environments were suggested.

This study contributes to the body of knowledge in the field of climbing robots because kinodynamic constraints were systematically analyzed and verified via simulations and experiments. Although these analyses are essential for climbing robots to perform real-life tasks in which falling or slipping may occur, previous studies involving climbing robots mainly investigated quasistatic movements without considering dynamics and did not apply analyses under kinodynamic constraints to the control algorithm.

Nevertheless, nonlinear disturbances during the adhesion or detachment of a robot complicate adhesion control near the ceiling. This disturbance should be further investigated in future studies, and an advanced control algorithm instead of the PD control can be employed to predict and impede the disturbance. When this investigation regarding nonlinear disturbances is completed, further studies focusing on robotics problems and industrial applications of the proposed robot system will be possible.

A future research direction in robotics is multirobot coordination between the base and adhesion robots [29], [30], which enables navigation and path planning of the climbing robot, similar to the proposal in Section V. Moreover, the proposed robot system can be used in industrial applications, such as the crack inspection process for social infrastructure. Considering the characteristics of the inspection process, human–robot interaction can be proposed, such as a tele-operation methodology to perform precise operations on air [31], [32], inspection methods using various deep learning technologies, or multimodal data fusion [33], [34]. Moreover, they can be applied to the proposed robot system to verify their effectiveness.

REFERENCES

[1] L. Briones, P. Bustamante, and M. A. Serna, "Wall-climbing robot for inspection in nuclear power plants," in *Proc. IEEE Int. Conf. Robot. Autom.*, vol. 2, May 1994, pp. 1409–1414.

[2] W. Lee, M. Hirai, and S. Hirose, "Gunryu III: Reconfigurable magnetic wall-climbing robot for decommissioning of nuclear reactor," *Adv. Robot.*, vol. 27, no. 14, pp. 1099–1111, Oct. 2013.

[3] K. Seo, S. Cho, T. Kim, J. Kim, and H. S. Kim, "Design and stability analysis of a novel wall-climbing robotic platform (ROPE RIDE)," *Mechanism Mach. Theory*, vol. 70, pp. 189–208, Dec. 2013, doi: 10.1016/j.mechmachtheory.2013.07.012.

[4] Y. Zhao, Z. Fu, Q. Cao, and Y. Wang, "Development and applications of wall-climbing robots with a single suction cup," *Robotica*, vol. 22, no. 6, pp. 643–648, Nov. 2004.

[5] L. Yang, B. Li, G. Yang, Y. Chang, Z. Liu, B. Jiang, and J. Xiaol, "Deep neural network based visual inspection with 3D metric measurement of concrete defects using wall-climbing robot," in *Proc. IEEE/RSJ Int. Conf. Intell. Robots Syst. (IROS)*, Nov. 2019, pp. 2849–2854.

[6] L. Yangi, G. Yang, Z. Liu, Y. Chang, B. Jiang, Y. Awad, and J. Xiao, "Wall-climbing robot for visual and GPR inspection," in *Proc. 13th IEEE Conf. Ind. Electron. Appl. (ICIEA)*, May 2018, pp. 1004–1009.

[7] Y. Yang and S. Nagarajaiah, "Dynamic imaging: Real-time detection of local structural damage with blind separation of low-rank background and sparse innovation," *J. Struct. Eng.*, vol. 142, no. 2, Feb. 2016, Art. no. 04015144.

[8] S.-N. Yu, J.-H. Jang, and C.-S. Han, "Auto inspection system using a mobile robot for detecting concrete cracks in a tunnel," *Autom. Construct.*, vol. 16, no. 3, pp. 255–261, 2007.

[9] W. Qi, S. E. Ovur, Z. Li, A. Marzullo, and R. Song, "Multi-sensor guided hand gesture recognition for a teleoperated robot using a recurrent neural network," *IEEE Robot. Autom. Lett.*, vol. 6, no. 3, pp. 6039–6045, Jul. 2021.

[10] L. V. Herlant, R. M. Holladay, and S. S. Srinivasa, "Assistive teleoperation of robot arms via automatic time-optimal mode switching," in *Proc. 11th ACM/IEEE Int. Conf. Hum.-Robot Interact. (HRI)*, Mar. 2016, pp. 35–42.

[11] S. Nansai and R. Mohan, "A survey of wall climbing robots: Recent advances and challenges," *Robotics*, vol. 5, no. 3, p. 14, Jul. 2016, doi: 10.3390/robotics5030014.

[12] B. Chu, K. Jung, C.-S. Han, and D. Hong, "A survey of climbing robots: Locomotion and adhesion," *Int. J. Precis. Eng. Manuf.*, vol. 11, no. 4, pp. 633–647, Aug. 2010.

[13] J. Hu, X. Han, Y. Tao, and S. Feng, "A magnetic crawler wall-climbing robot with capacity of high payload on the convex surface," *Robot. Auto. Syst.*, vol. 148, Feb. 2022, Art. no. 103907, doi: 10.1016/j.robot.2021.103907.

[14] H. Zhang, J. Zhang, G. Zong, W. Wang, and R. Liu, "Sky cleaner 3: A real pneumatic climbing robot for glass-wall cleaning," *IEEE Robot. Autom. Mag.*, vol. 13, no. 1, pp. 32–41, Mar. 2006, doi: 10.1109/MRA.2006.1598051.

[15] S. Kim, M. Spenko, S. Trujillo, B. Heyneman, D. Santos, and M. R. Cutkosky, "Smooth vertical surface climbing with directional adhesion," *IEEE Trans. Robot.*, vol. 24, no. 1, pp. 65–74, Feb. 2008.

[16] G. Andrikopoulos, A. Papadimitriou, A. Brusell, and G. Nikolakopoulos, "On model-based adhesion control of a vortex climbing robot," in *Proc. IEEE/RSJ Int. Conf. Intell. Robots Syst. (IROS)*, Nov. 2019, pp. 1460–1465.

[17] G. Lee, G. Wu, J. Kim, and T. Seo, "High-payload climbing and transitioning by compliant locomotion with magnetic adhesion," *Robot. Auto. Syst.*, vol. 60, no. 10, pp. 1308–1316, Oct. 2012, doi: 10.1016/j.robot.2012.06.003.

[18] S. Nam, J. Oh, G. Lee, J. Kim, and T. Seo, "Dynamic analysis during internal transition of a compliant multi-body climbing robot with magnetic adhesion," *J. Mech. Sci. Technol.*, vol. 28, no. 12, pp. 5175–5187, Dec. 2014, doi: 10.1007/s12206-014-1141-z.

[19] Y. Guan, H. Zhu, W. Wu, X. Zhou, L. Jiang, C. Cai, L. Zhang, and H. Zhang, "A modular biped wall-climbing robot with high mobility and manipulating function," *IEEE/ASME Trans. Mechatronics*, vol. 18, no. 6, pp. 1787–1798, Dec. 2013, doi: 10.1109/TMECH.2012.2213303.

[20] Y. Guan, L. Jiang, H. Zhu, W. Wu, X. Zhou, H. Zhang, and X. Zhang, "Climbot: A bio-inspired modular biped climbing robot—System development, climbing gaits, and experiments," *J. Mech. Robot.*, vol. 8, no. 2, Apr. 2016, Art. no. 021026, doi: 10.1115/1.4028683.

[21] Y.-W. Song, T. Kim, M. Lee, S. Rho, J. Kim, J. Kang, and S.-C. Yu, "Development of safety-inspection-purpose wall-climbing robot utilizing aerial drone with lifting function," in *Proc. 18th Int. Conf. Ubiquitous Robots (UR)*, Jul. 2021, pp. 411–416.

[22] Y.-W. Song, J. Kang, T. Kim, and S.-C. Yu, "Multi-agent-based wall-climbing robot system for safety inspection of nuclear power plant," in *Proc. Decommissioning Environ. Sci. Remote Technol.*, Dec. 2021, pp. 104–107.

[23] J. Xiao, A. Calle, A. Sadegh, and M. Elliott, "Modular wall climbing robots with transition capability," in *Proc. IEEE Int. Conf. Robot. Biomim. (ROBIO)*, Jul. 2005, pp. 246–250.

[24] B. Donald, P. Xavier, J. Canny, and J. Reif, "Kinodynamic motion planning," *J. ACM*, vol. 40, no. 5, pp. 1048–1066, Nov. 1993.

[25] G. Andrikopoulos and G. Nikolakopoulos, "Design, development and experimental evaluation of a vortex actuation system," in *Proc. 14th IEEE/ASME Int. Conf. Mech. Embedded Syst. Appl. (MESA)*, Jul. 2018, pp. 1–6.

[26] H. Pacejka, "Basic tire modeling considerations," in *Tire and Vehicle Dynamics*. Oxford, U.K.: Butterworth-Heinemann, 2012, pp. 59–85.

[27] S. Hamaza, I. Georgilas, G. Heredia, A. Ollero, and T. Richardson, "Design, modeling, and control of an aerial manipulator for placement and retrieval of sensors in the environment," *J. Field Robot.*, vol. 37, no. 7, pp. 1224–1245, Jun. 2020, doi: 10.1002/rob.21963.

[28] H. Lee, B. Yu, C. Tirtawardhana, C. Kim, M. Jeong, S. Hu, and H. Myung, "CAROS-Q: Climbing aerial RObot system adopting rotor offset with a quasi-decoupling controller," *IEEE Robot. Autom. Lett.*, vol. 6, no. 4, pp. 8490–8497, Oct. 2021, doi: 10.1109/LRA.2021.3108489.

[29] Z. Yan, N. Jouandeau, and A. A. Cherif, "A survey and analysis of multi-robot coordination," *Int. J. Adv. Robot. Syst.*, vol. 10, no. 12, pp. 399–416, 2013.

[30] R. Doriya, S. Mishra, and S. Gupta, "A brief survey and analysis of multi-robot communication and coordination," in *Proc. Int. Conf. Comput., Commun. Autom.*, May 2015, pp. 1014–1021.

[31] W. Qi, H. Su, J. Zhang, R. Song, G. Ferrigno, E. De Momi, and A. Aliverti, "Active learning strategy of finger flexion tracking using sEMG for robot hand control," in *Proc. 6th IEEE Int. Conf. Adv. Robot. Mechatronics (ICARM)*, Jul. 2022, pp. 753–758.

[32] T. Zhou, Q. Zhu, and J. Du, "Intuitive robot teleoperation for civil engineering operations with virtual reality and deep learning scene reconstruction," *Adv. Eng. Inform.*, vol. 46, Oct. 2020, Art. no. 101170.

[33] W. Qi and A. Aliverti, "A multimodal wearable system for continuous and real-time breathing pattern monitoring during daily activity," *IEEE J. Biomed. Health Informat.*, vol. 24, no. 8, pp. 2199–2207, Aug. 2020.

[34] S. Papanastasiou, N. Kousi, P. Karagiannis, C. Gkournelos, A. Papavasileiou, K. Dimoulas, K. Baris, S. Koukas, G. Michalos, and S. Makris, "Towards seamless human robot collaboration: Integrating multimodal interaction," *Int. J. Adv. Manuf. Technol.*, vol. 105, no. 9, pp. 3881–3897, Dec. 2019.

YOUNG-WOON SONG received the B.S. degree from the Department of Creative IT Engineering, Pohang University of Science and Technology (POSTECH), Pohang, South Korea, in 2019, where he is currently pursuing the Ph.D. degree in convergence IT engineering. His research interests include field robotics, underwater robots, and robot control.

JUNGILL KANG is currently pursuing the B.S. degree in convergence IT engineering with the Pohang University of Science and Technology (POSTECH), Pohang, South Korea. His research interests include robot control and simulations.

SON-CHEOL YU (Member, IEEE) received the M.E. and Ph.D. degrees from the Department of Ocean and Environmental Engineering, The University of Tokyo, in 2000 and 2003, respectively.

He is currently a Professor at the Division of Advanced Nuclear Engineering, Department of Convergence IT Engineering and Electrical Engineering, Pohang University of Science and Technology (POSTECH), South Korea. He is also the Director of the Hazardous and Extreme Environment Robotics Laboratory (HERO Lab), the IEEE Ocean Engineering Society Korea Chapter, and the Gyeongbuk Sea Grant Center. His research interests include autonomous underwater vehicles, intelligent sensing, and multi-agent robot systems.

• • •